

Electrically controlled all-antiferromagnetic tunnel junctions on silicon with large room-temperature magnetoresistance

Jiacheng Shi¹, Sevdenur Arpacı^{1,2}, Victor Lopez-Dominguez^{1,3}*, Vinod K. Sangwan⁴, Farzad Mahsouzi⁵, Jinwoong Kim⁵, Jordan G. Athas¹, Mohammad Hamdi¹, Can Aygen¹, Hanu Arava⁶, Charudatta Phatak⁶, Mario Carpentieri⁷, Jidong S. Jiang⁶, Matthew A. Grayson^{1,2}, Nicholas Kioussis⁵*, Giovanni Finocchio⁸*, Mark C. Hersam^{1,2,4,9}, Pedram Khalili Amiri^{1,2}**

Affiliations:

¹ Department of Electrical and Computer Engineering, Northwestern University; Evanston, Illinois 60208, United States of America.

² Applied Physics Program, Northwestern University; Evanston, Illinois 60208, United States of America.

³ Institute of Advanced Materials (INAM), Universitat Jaume I; Castellón, 12006, Spain.

⁴ Department of Materials Science and Engineering, Northwestern University; Evanston, Illinois 60208, United States of America.

⁵ Department of Physics and Astronomy, California State University Northridge; Northridge, California 91330, United States of America.

⁶ Materials Science Division, Argonne National Laboratory; Lemont, Illinois 60439, United States of America.

⁷ Department of Electrical and Information Engineering, Politecnico di Bari; Bari, Italy.

⁸ Department of Mathematical and Computer Sciences, Physical Sciences and Earth Sciences, University of Messina; Messina 98166, Italy.

⁹ Department of Chemistry, Northwestern University; Evanston, Illinois 60208, United States of America.

* Email: victor.lopez@uji.es, nick.kioussis@csun.edu, gfinocchio@unime.it, pedram@northwestern.edu

⁵ These authors contributed equally to this work.

Keywords: Antiferromagnets, magnetic random-access memory, magnetic tunnel junctions, tunneling magnetoresistance, spin-orbit torques, silicon.

1 **Abstract:** Antiferromagnetic (AFM) materials are a pathway to spintronic memory and computing
2 devices with unprecedented speed, energy efficiency, and bit density. Realizing this potential
3 requires AFM devices with simultaneous electrical writing and reading of information, which are
4 also compatible with established silicon-based manufacturing. Recent experiments have shown
5 tunneling magnetoresistance (TMR) readout in epitaxial AFM tunnel junctions. However, these
6 TMR structures were not grown using a silicon-compatible deposition process, and controlling
7 their AFM order required external magnetic fields. Here we show three-terminal AFM tunnel
8 junctions based on the noncollinear antiferromagnet PtMn_3 , sputter-deposited on silicon. The
9 devices simultaneously exhibit electrical switching using electric currents, and electrical readout
10 by a large room-temperature TMR effect. First-principles calculations explain the TMR in terms
11 of the momentum-resolved spin-dependent tunneling conduction in tunnel junctions with
12 noncollinear AFM electrodes.

13 **Introduction**

14 Antiferromagnetic (AFM) materials have unique advantages such as robustness against external
15 magnetic fields, high-frequency dynamics at picosecond time scales, and vanishing net
16 macroscopic magnetization, attracting the interest of the semiconductor industry. These properties
17 may enable the next generation of memory and computing devices with unprecedented speed,
18 energy efficiency, and bit density, as well as resonant electrically tunable terahertz detectors and
19 emitters¹⁻¹⁰.

20 Recent studies have established the possibility of using electric currents, by means of spin-
21 orbit torque (SOT), to manipulate magnetic order in AFM thin films and heterostructures^{5, 11-23}.
22 However, the practical realization of AFM memory devices requires mechanisms for *both*
23 *manipulation and detection* of AFM order by electrical means. Until recently, the electrical
24 detection of the magnetic state in AFM structures exclusively relied on the anisotropic
25 magnetoresistance (AMR) and spin Hall magnetoresistance (SMR) effects, which provided
26 relative resistance variations ($\Delta R/R$) that were too small for memory applications^{24, 25}.

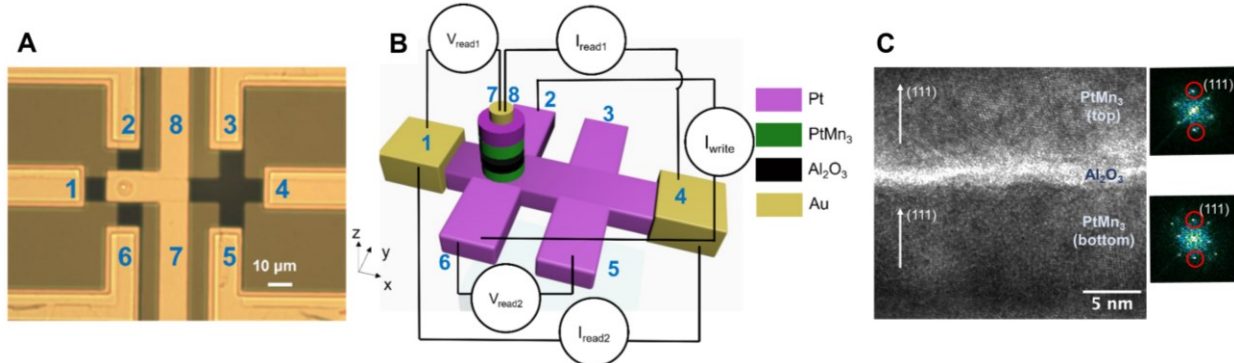
27 One approach to solving this readout issue is to utilize tunneling effects, which in the case of
28 ferromagnetic (FM) devices, have been previously shown to provide substantially larger $\Delta R/R$
29 values^{26, 27}. In addition, this type of readout can, in principle, be combined with SOT in a three-
30 terminal device structure, providing separate electrical paths for writing and reading of
31 information. A recent work demonstrated that an AFM state, switched by SOT, can be imprinted
32 on an adjacent ferromagnetic layer for readout by TMR²³. The presence of a ferromagnetic tunnel
33 junction within the device, however, eliminates some of the potential advantages of an AFM
34 memory listed above. Realizing large TMR effects in all-AFM tunnel junctions, however, is a
35 significantly greater challenge compared to the ferromagnetic case, due to the absence of
36 macroscopic magnetization in antiferromagnets.

37 Two general approaches have been proposed to address this challenge. The first involves so-
38 called altermagnetic materials^{28, 29}, which have collinear moments and a staggered spin structure
39 in both real and momentum space, giving rise to unconventional spin current generation in the
40 presence of electric charge currents^{30, 31}. The second approach, adopted here, involves
41 noncollinear antiferromagnets of the XMn_3 family. These materials feature a helicity of the spin
42 polarization in momentum space, which was recently predicted to result in sizeable dependence of
43 the tunneling conduction on the Néel vector orientation in noncollinear AFM-based tunnel
44 junctions, *i.e.*, the fully antiferromagnetic analogue of the TMR effect³².

45 While this latter effect has been recently observed in all-AFM tunnel junctions based on PtMn_3
46³³ and SnMn_3 ³⁴, these experiments relied on fabrication processes that are difficult to scale, namely

1 epitaxially grown single-crystal films on non-silicon substrates (MgAl_2O_4 and MgO , respectively).
 2 In addition, their AFM order was manipulated by using large external magnetic fields, making
 3 them impractical for electronic memory devices, which require an all-electrical read and write
 4 protocol.

5 Here we demonstrate the first all-antiferromagnetic tunnel junction (AATJ) devices with high
 6 TMR, grown via a scalable sputter deposition on conventional thermally oxidized silicon
 7 substrates. The three-terminal device has an all-electrical read and write protocol, whereby the
 8 magnetic state of the non-collinear antiferromagnetic PtMn_3 free layer is electrically written by
 9 current-induced SOT, in the absence of any external magnetic fields, and is subsequently read by
 10 using the TMR effect. The devices exhibit SOT-controlled TMR ratios as large as 110%. In this
 11 device structure, illustrated in Fig. 1, an Al_2O_3 tunnel barrier separates a fixed PtMn_3 top AFM
 12 layer from a free PtMn_3 bottom AFM layer, which has a predominant [111] texture due to being
 13 grown on a Pt seed layer, which also acts as the source of SOT. All layers are grown using sputter
 14 deposition at room temperature. We chose PtMn_3 due to its robust room-temperature non-collinear
 15 antiferromagnetic phase, which remains stable up to ~ 400 K before transitioning to a collinear
 16 phase, with a Néel temperature of ~ 475 K³⁵. We compare these results to AMR-based differential
 17 voltage measurements in the same device structure using a previously developed measurement
 18 protocol¹⁷, which reveal a $10^3\times$ enhancement of the room-temperature resistive readout signal
 19 when using the TMR readout mechanism. Additional current-induced switching measurements,
 20 performed on reference tunnel junction devices without the AFM elements, confirm the magnetic
 21 origin of the switching signal.



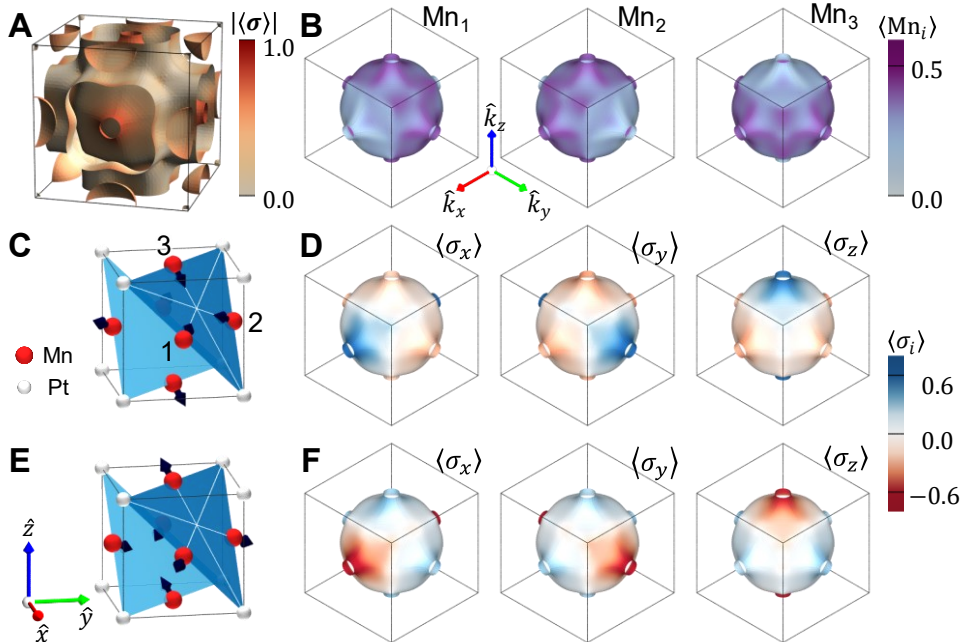
22
 23 **Fig. 1. Layout and device structure of the PtMn_3 -based three-terminal antiferromagnetic tunnel junctions.** **A**,
 24 Optical microscope image of the device. Note that the tunnel junction is covered by the top electrodes 7 and 8.
 25 Electrodes 1 through 6 are bottom electrodes. **B**, Schematic and measurement configuration of the three-terminal
 26 tunnel junctions. The write current is applied between electrodes 2 and 6 with opposite directions, exerting spin-orbit
 27 torque on the bottom PtMn_3 free AFM layer, which is in direct contact with the underlying Pt layer. Terminals 3 and
 28 5 are used for control experiments to verify that the observed switching signals originate from the PtMn_3 . Read currents
 29 $I_{\text{read}1}$ and $I_{\text{read}2}$ are applied to sense the average Néel vector configuration using tunneling resistance (TR) and
 30 differential voltage (DV) measurements, respectively. **C**, High-resolution transmission electron microscopy (HRTEM)
 31 image of the cross-section of the $\text{PtMn}_3/\text{Al}_2\text{O}_3/\text{PtMn}_3$ structure, showing the [111] preferred orientation of the grains
 32 in each PtMn_3 layer determined from the diffractograms.

33 Origin of TMR in $\text{PtMn}_3/\text{Al}_2\text{O}_3/\text{PtMn}_3$ tunnel junctions

34 Unlike conventional ferromagnet-based tunnel junctions where TMR can be straightforwardly
 35 understood in terms of the free layer magnetization direction, the chiral nature of noncollinear
 36 (NC) antiferromagnets can also give rise to TMR, even in the absence of a net macroscopic
 37 magnetization. The necessary ingredients for TMR in spin-neutral tunnel junctions containing NC-
 38

1 AFM layers are (*i*) the non-relativistic momentum-dependent spin polarization resulting from the
 2 noncollinear magnetic ordering^{32, 33}, and (*ii*) the conservation of the tunneling electron's
 3 momentum parallel to the transport direction, $\vec{k}_{||}$. In this case, the spin polarization of the tunneling
 4 current at each $\vec{k}_{||}$ -point contributes a finite, and overall positive, value to the total TMR.

5 Figure 2 shows the spin polarization of the Fermi surface in bulk PtMn₃. Fig. 2A shows the
 6 Fermi surfaces, where the color intensity shows the amplitude of the expectation value of the spin
 7 operator. We focus on the Fermi surface of the band which exhibits the strongest spin polarization
 8 amplitude as shown in Fig. 2B, where the color intensity illustrates the amplitude of the projection
 9 of the electronic eigenstates on the three Mn atoms in the unit cell. Here, the magnetic moments
 10 of Mn₁, Mn₂ and Mn₃ atoms are oriented either parallel (state 1) or anti-parallel (state 2) to the
 11 [2̄11], [1̄21], and [11̄2] directions, respectively. It is, therefore, expected that the spin
 12 polarizations of the eigenstates follow the projection value of the state on each Mn atom. As an
 13 example, the large amplitude in the spin polarization, $\langle \sigma_x \rangle$ (i.e., dark blue region on the left panel
 14 in Fig. 2D) is associated with the Mn₂ and Mn₃ atoms. The same region exhibits negative half
 15 amplitude (pale red color) in $\langle \sigma_y \rangle$ and $\langle \sigma_z \rangle$ projections, consistent with the direction of a mutual
 16 net magnetic moment, $\vec{M}(\text{Mn}_2) + \vec{M}(\text{Mn}_3) = -\vec{M}(\text{Mn}_1) \parallel [2\bar{1}\bar{1}]$. The noncollinear spin
 17 configuration of the Mn atoms is then expected to yield momentum-dependent spin polarization
 18 which is shown in Figs. 2D and 2F, corresponding to the two opposite magnetic states depicted in
 19 Figs. 2C and 2E, respectively.



20
 21 **Fig. 2. Fermi surface and spin/atom-projected density of states in PtMn₃.** **A**, Fermi surfaces in the first Brillouin
 22 zone with net spin polarization shown as color intensity. **B**, Projected orbital characters at each Mn site (Mn₁, Mn₂,
 23 Mn₃) of the selected band with the highest spin polarization amplitude. **C, E**, Magnetic configurations of states 1 and
 24 2, corresponding to opposite magnetizations of all three sublattices, respectively. The black arrows of the Mn_{*i*} (*i* =
 25 1,2,3) atoms denote the magnetic moment along the [2̄11], [1̄21], and [11̄2] directions (white lines). **D, F**, Projected
 26 spin texture ($\langle \sigma_x \rangle$, $\langle \sigma_y \rangle$, $\langle \sigma_z \rangle$) on the selected band of states 1 and 2, respectively.

27
 28 To evaluate the expected TMR ratio emerging from this momentum-dependent spin

polarization mechanism in NC-AFM tunnel junctions, we performed *ab initio* electronic structure calculations for a tunnel junction composed of PtMn₃ electrodes and a 1.7 nm α -Al₂O₃ barrier. The spin configuration was initialized and constrained in the [111] plane, as shown in the relaxed structure depicted in Fig. 3A. We employed the Landauer-Buttiker expression ³⁶ to calculate the transmission across the tunnel junction for both parallel (T_P) and anti-parallel (T_{AP}) cases. Previous *ab initio* calculations ^{32, 33} of TMR in noncollinear AFM tunnel junctions employed as a barrier either vacuum or a monolayer of HfO₂. However, these choices might not accurately represent the $\vec{k}_{||}$ -resolved electron tunneling phenomenon. In contrast, the calculations reported in this work utilize an α -Al₂O₃ barrier which aligns more closely with our experimental structure. The results for the transmissions as a function of the shift of the chemical potential in PtMn₃ in these two magnetic configurations are depicted in Fig. 3B, as blue and green lines, respectively. The inset shows the corresponding TMR values computed from $TMR = (T_P - T_{AP})/T_{AP}$. The result shows a positive TMR up to 300%, with an average of 100% in the undoped PtMn₃ case. Figs. 3C and 3D show the k -resolved transmission in the parallel and anti-parallel cases, respectively. The results suggest that transmissions have 6-fold (C₆) symmetry consistent with the hexagonal symmetry of the crystal structure and are peaked near the Γ -point. In Fig. 3E, we present the k -resolved TMR, $TMR_{\vec{k}} = (T_P^{\vec{k}} - T_{AP}^{\vec{k}})/T_{AP}^{\vec{k}}$. The result demonstrates that there is a cancellation of the transmission for k -points closer to the Γ -point, due to the absence of spin polarization near the Γ -point.

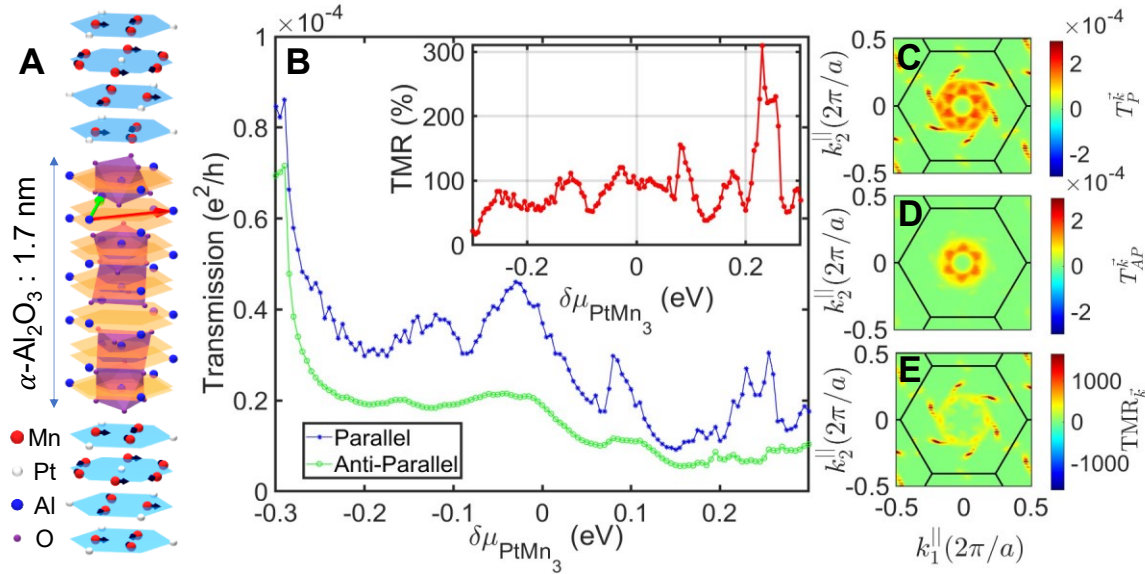


Fig. 3. Crystal structure and *ab initio* results for TMR in PtMn₃[111]/Al₂O₃/PtMn₃[111] tunnel junctions. **A**, Relaxed crystal structure of the 1.7 nm α -Al₂O₃ barrier sandwiched between two semi-infinite PtMn₃ leads grown along the [111] direction. The magnetic moments of the noncollinear AFM are in-plane, consistent with the experiments shown later in the text, and are indicated as arrows in the parallel (P) configuration. In the anti-parallel (AP) configuration, the magnetic moments of the bottom PtMn₃ film are flipped. **B**, *Ab initio* results for the transmission through the tunnel junction for P (blue) and AP (green) configurations versus the chemical potential of PtMn₃. The inset (red) shows the calculated TMR as a function of the chemical potential of PtMn₃. **C**, **D**, k -resolved transmission at the Fermi level, $\delta\mu_{PtMn_3} = 0$, for parallel and anti-parallel configurations, respectively. **E**, k -resolved TMR at the Fermi level calculated by the difference of the k -resolved transmissions in P and AP configurations, divided by the total transmission in the AP case. The thick black lines depict the edge of the first Brillouin zone.

1

2 Device structure and measurement configurations

3 Figures 1A and 1B show an optical micrograph and a schematic of the three-terminal AATJ
4 devices. Here, the main device structure is composed of the three terminals 2, 6, and 7 (or 8), while
5 all other terminals are used for control experiments, as outlined below. The material stack consists
6 of a Pt(5)/PtMn₃(10)/Al₂O₃(2)/PtMn₃(10)/Pt(5) layered structure (thicknesses in brackets are
7 expressed in nanometers), where all materials are sputter-deposited on a thermally oxidized silicon
8 substrate, making them compatible with conventional semiconductor manufacturing processes.
9 The devices were constructed by patterning the as-deposited AATJ films by photolithography into
10 pillars with diameters of 6 and 8 μm on top of the bottom Pt(5) layer, which was patterned into a
11 double-cross structure with six electrodes. The PtMn₃ tunnel junction pillar was placed at the
12 center of one of the crosses (between electrodes 2 and 6, as shown in Fig. 1B). The bottom Pt layer
13 acts as an SOT source to electrically manipulate the PtMn₃ AFM order, when a write current pulse
14 of 1 ms width is applied between electrodes 2 and 6, as shown in Fig. 1B.

15 Figure 1C shows the high-resolution transmission electron microscopy (HRTEM) image of
16 the AATJ stack. It can be observed that the Al₂O₃ layer is amorphous and continuous, although
17 with relatively large roughness. The average thickness of the Al₂O₃ film is close to 2 nm. The
18 PtMn₃ films are polycrystalline. We estimated the height of the Al₂O₃ tunnel barrier to be \sim 1.57
19 eV, by using current versus voltage curves measured across the tunnel junction, following an
20 approach similar to previous works³⁷. This value is in good agreement with previous reports on
21 Al₂O₃ barriers^{38, 39}. The diffractograms from various grains in the PtMn₃ films (top and bottom)
22 were analyzed, two of which are shown in Fig. 1C. From these diffractograms, it can be determined
23 that the grains have a preferred [111] orientation along the growth direction. The PtMn₃ free layer
24 has a non-collinear L1₂ phase and a Mn:Pt ratio of \sim 3.2, as revealed by X-ray diffraction (XRD)
25 and X-ray photoelectron spectroscopy (XPS) measurements. The AFM character of the PtMn₃
26 layer was confirmed by characterizing the exchange bias in a thin Co layer adjacent to it. These
27 structural and magnetic characterization data are provided in Supplementary Note 1.

28 Two types of measurements were used to read out the state of the AFM pillar in this device:
29 (i) Tunneling resistance (TR) measurements, where a read current I_{read1} is applied through the
30 tunnel junction via terminals 4 and 7, while the readout voltage V_{read1} is measured using terminals
31 1 and 8; (ii) Differential voltage (DV) measurement, where a read current I_{read2} is applied through
32 the underlying Pt via terminals 1 and 4, while the readout voltage V_{read2} is measured using terminals
33 5 and 6, following a previously developed differential measurement protocol¹⁷. The DV
34 measurements were used as an independent readout method, which confirms the magnetic origin
35 of the observed current-induced switching signals in our devices. The separation of the electrical
36 read and write paths of the device, as indicated in Fig. 1B, is beneficial for memory applications
37 as it prevents deterioration of the tunneling barrier due to repeated write attempts, while also
38 reducing the chance of changing the magnetic state during reading (*i.e.*, read disturbance).

39

40 Tunneling resistance measurement results

41 The tunneling resistance was measured at room temperature after each electrical switching attempt,
42 which consisted of applying ten consecutive 1 ms writing current pulses from electrode 2 to 6 and
43 reversing the current pulse direction, from electrodes 6 to 2. Figure 4A shows the results for the
44 TR measurement in a device with a 6 μm diameter AFM pillar. A clear current-induced switching
45 signal is observed for a write current amplitude of 33 mA. The device exhibits a TMR ratio \sim

110%, defined as $\Delta R/R = (R_{\text{high}} - R_{\text{low}})/R_{\text{low}}$, where R_{high} and R_{low} are the high and low AATJ resistance levels observed in the experiment. Using the R_{low} value of $\sim 60 \Omega$, one can estimate the resistance-area product of the junction to be $\sim 1.7 \text{ k}\Omega\text{-}\mu\text{m}^2$. We emphasize that no magnetic fields were applied during this experiment. Supplementary Note 2 shows TMR switching measurements on two additional devices, which are in qualitative agreement with the results of Fig. 4.

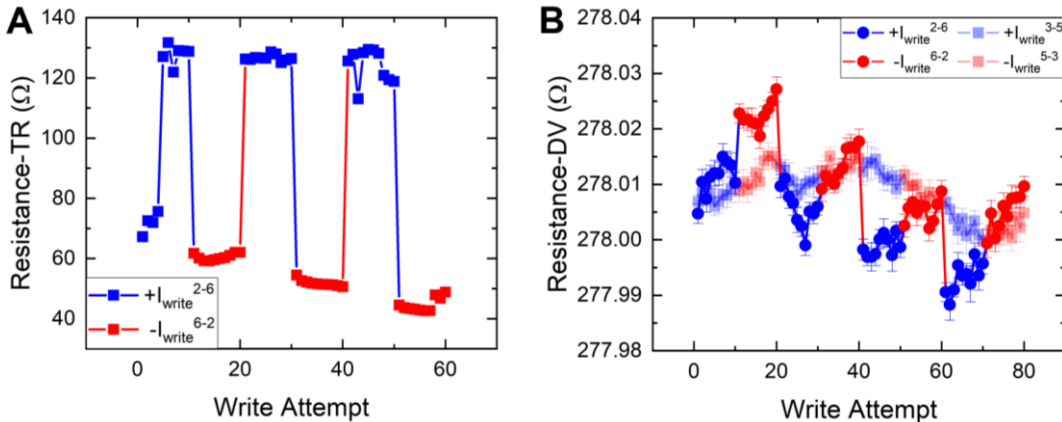


Fig. 4. Electrical readout of the SOT-switched PtMn_3 state by using tunneling resistance (TR) and differential voltage (DV) measurements. A, TR measurement results in a $6 \mu\text{m}$ diameter AATJ. Each write attempt in this case used a current amplitude of 33 mA , applied between electrodes 2 and 6. B, DV measurement results in the same structure (dark blue and red data points) also exhibit switching of the PtMn_3 , but with a much smaller amplitude due to the smaller AMR effect. The background resistance of $\sim 278 \Omega$ is associated with the thin Pt bottom layer. Control experiments were performed in the form of DV measurements in the same device, but with write currents sent along the non-magnetic arm between electrodes 3 and 5 (light blue and red data points). As expected, no switching is observed in this case, confirming the magnetic origin of the TMR and AMR switching signals in our experiment.

Differential voltage measurements and control experiments

In addition to TR, DV measurements were performed where a reading current of $10 \mu\text{A}$ was applied from electrode 1 to 4, and the differential voltage was measured between electrodes 5 and 6, thus, revealing changes in the AFM Néel vector via the AMR effect. The DV measurement provides an independent test to rule out non-magnetic artifacts in the resistive switching signal^{17, 24, 25}. In fact, when repeating the switching experiments using the same write current in terminals 3 and 5 of Fig. 1, *i.e.*, without the AFM element, we observed no current-induced switching in the DV measurements. This result, which is summarized in Fig. 4B, rules out the contribution of non-magnetic artifacts in the observed switching.

Note that the background resistance observed in the DV measurements of Fig. 4B is significantly larger than in the TR experiments, due to the high resistance of the long and ultrathin Pt arm of the device from electrode 1 to 4. The resistance variation in this case is estimated to be $\Delta R \sim 20 \text{ m}\Omega$, which is more than three orders of magnitude smaller than that measured with the TR method, clearly confirming the superiority of the tunneling measurement as the readout mechanism.

To further confirm the magnetic origin of the TMR switching signals, we also carried out current-induced switching experiments on control tunnel junction devices without any AFM element (*i.e.*, Pt/Al₂O₃/Pt devices). The results are shown in Supplementary Note 3, indicating no switching signals in the non-magnetic control experiments, as expected.

The described switching experiments were carried out on 12 AATJs made from the same tunnel

junction material stack, all of which showed qualitatively similar results using write currents ranging from 32 to 36 mA. The distributions of all $\Delta R/R$ and ΔR values obtained from the TR and DV measurements are shown in Figs. 5A and 5B, respectively, indicating an average increase of the resistive readout signal by more than $10^3 \times$ when using the tunnel junction readout. The $\Delta R/R$ ratio differences between the devices can be attributed to device-to-device variations induced by the fabrication process, as well as variations in the local magnetic anisotropy and domain structure, which in turn can affect the critical current required for switching of each device, as well as the micromagnetic structure of the fixed layer. The role of nonuniformities of the PtMn_3 magnetic anisotropy on the observed switching characteristics is supported by micromagnetic simulations, which are shown in Supplementary Note 4. Qualitatively, the current-induced switching is similar to previous reports in other metallic antiferromagnets^{15, 17}, where micromagnetic simulations indicated a reversible modification of the average Néel vector in the device due to domain rotation and domain wall motion in response to opposite current pulses. We expect that a similar mechanism exists in the present experiment.

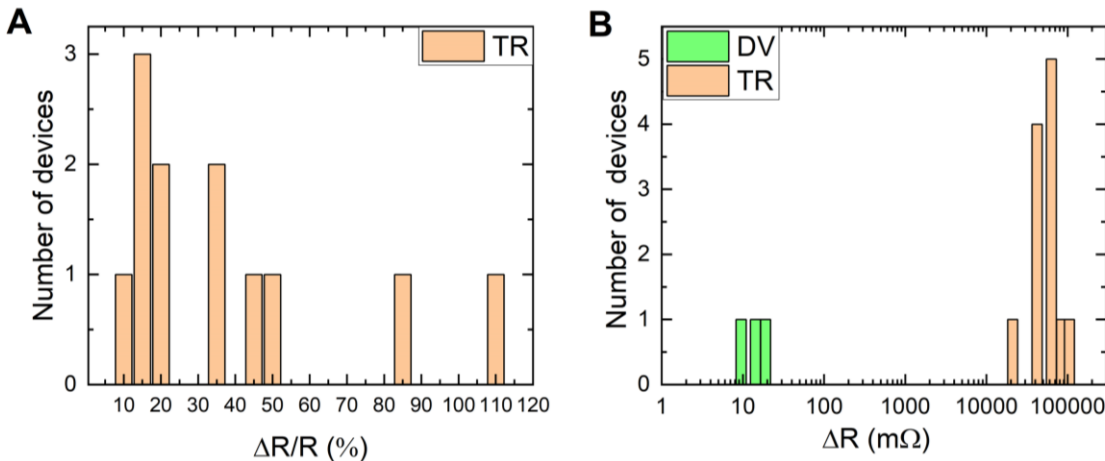


Fig. 5. Statistics of the AFM state readout using TR and DV measurements. A, Distribution of the $\Delta R/R$ ratio over all 12 devices measured in this work. The largest observed TMR ratio was $\sim 110\%$. All data were measured at room temperature and in the absence of any external magnetic fields. B, Comparison of ΔR values from TR and DV measurements. The mean ΔR increases by more than $10^3 \times$ when using the tunnel junction readout.

Discussion

It is worth comparing these results to previous reports of TMR in antiferromagnet-based tunnel junctions, where manipulation of the magnetic order was performed by a magnetic field, rather than by electric currents. A related effect, tunneling anisotropic magnetoresistance (TAMR), was first experimentally observed in AFM tunnel junctions with $[\text{Co}/\text{Pt}]/\text{Ir}-\text{Mn}/\text{AlO}_x/\text{Pt}$ and $\text{NiFe}/\text{Ir}-\text{Mn}/\text{MgO}/\text{Pt}$ ⁴⁰⁻⁴² material structures. In these experiments, manipulation of the AFM order was implemented using an external magnetic field, through the exchange coupling of the ferromagnetic (Co/Pt or NiFe) and antiferromagnetic (Ir-Mn) layers in the device. These structures showed TAMR only at cryogenic temperatures⁴⁰ due to the exceptionally thin AFM layers that were required to make the magnetic-field-controlled manipulation mechanism possible, thus reducing their Néel temperature below room temperature.

Two recent reports have demonstrated room-temperature TMR, controlled by external magnetic fields, in all-AFM tunnel junctions based on PtMn_3 ³³ and SnMn_3 ³⁴ noncollinear antiferromagnets. The material stacks were epitaxially grown on MgAl_2O_4 and MgO substrates,

1 respectively. In all of these cases, the need for external magnetic fields to manipulate the AFM
2 order reduced their potential as memory devices, which require an all-electrical protocol for
3 reading and writing of information. It is worth noting that a similar but smaller magnetoresistive
4 effect has also been observed in composite films where SnMn_3 grains were separated by Ag
5 spacers, rather than a tunnel barrier⁴³.

6 Another recent work demonstrated the possibility of imprinting the antiferromagnetic state of
7 an Ir-Mn layer, which is switched by current-induced spin-orbit torque, onto a ferromagnetic
8 CoFeB film²³. The resulting change in the ferromagnetic order can then be read out by using
9 conventional ferromagnetic TMR in a CoFeB/MgO/CoFeB tunnel junction. However, while
10 providing both electrical writing and reading functions, the need for a ferromagnetic layer in these
11 structures results in a finite magnetic dipole coupling of adjacent bits in a memory array and limits
12 their ultimate achievable switching speed and bit density, thus partly negating the attractive
13 features of using an AFM free layer in the device.

14 It is worth emphasizing that even though epitaxial PtMn_3 films have been shown to also exhibit
15 a collinear phase at elevated temperatures ($> \sim 400$ K), such a collinear antiferromagnetic phase is
16 neither expected to exist in our samples, nor would it be consistent with the observations of TMR
17 and anomalous Hall effect. In particular, the observed anomalous Hall effect in our samples
18 (shown in Supplementary Note 1) indicates the presence of a noncollinear phase³⁵. In addition,
19 the collinear phase is unstable in disordered films and at higher Mn:Pt ratios⁴⁴, which rules out its
20 presence in our polycrystalline samples. Furthermore, the collinear phase is not expected to give
21 rise to TMR either, since only the noncollinear phase has spin-split energy bands.

22 Given the surge of interest in the newly identified class of collinear AFMs called altermagnets,
23 which potentially do show TMR^{28, 30, 45}, a brief discussion is warranted to explain why symmetry
24 arguments preclude the existence of such a phase in PtMn_3 . Conventional collinear
25 antiferromagnets have either \mathbf{PT} symmetry or $t_{1/2}\mathbf{T}$ symmetry, where \mathbf{T} is time reversal, \mathbf{P} is
26 inversion, and $t_{1/2}$ is a half-unit cell translation. Thus, their opposite-spin sublattices are connected
27 by inversion or translation symmetry and exhibit \mathbf{T} -invariant spin-degenerate bands reminiscent
28 of nonmagnetic materials^{28, 45}. In sharp contrast, the \mathbf{PT} or $t_{1/2}\mathbf{T}$ symmetry is broken in
29 altermagnets, where their opposite spin sublattices are connected by rotation, not via translation or
30 inversion, and thus they have \mathbf{T} -breaking momentum-dependent band spin splitting^{28, 45}. Neutron
31 scattering experiments on bulk samples⁴⁴ and first-principles electronic structure calculations⁴⁶
32 have shown that bulk PtMn_3 undergoes a first transition between two AFM phases, where the low-
33 temperature ($< \sim 400$ K) phase (D-phase) is noncollinear while the high-temperature (~ 400 K $< T$
34 < 475 K) collinear AFM phase (F-phase) adopts a tetragonal crystal structure with \mathbf{PT} symmetry,
35 indicating the absence of spin-splitting in the band structure. Therefore, the substantial TMR
36 signals observed in our experiments suggest that the samples predominantly exhibit noncollinear
37 ordering in the D-phase.

38 39 Conclusions

40 The three-terminal AATJs reported in the present work combine three key properties required for
41 AFM memory device applications, which had not been realized simultaneously in previous works:
42 Firstly, they feature room-temperature all-electrical readout of the AFM state using large TMR
43 ratios, without the assistance of any ferromagnetic layers. Secondly, the AATJs exhibit magnetic-
44 field-free device operation, featuring electrical control of the AFM order by current-induced SOT.
45 Thirdly, this work demonstrates the integration of these all-AFM tunnel junction devices on a
46 conventional silicon substrate using scalable sputter deposition.

1 Together, these attributes enable electrical writing and reading in an industry-relevant three-
2 terminal device geometry with separate read and write paths. In addition to their significance as a
3 fully functional all-AFM memory on silicon, the field-free operation of these devices also presents
4 a significant advantage over ferromagnetic SOT memory devices, where achieving field-free
5 operation is currently an intensely researched and challenging problem⁴⁷⁻⁵⁵.

6 There is significant room for further development of AATJ structures based on the general
7 concept presented in this work, e.g., by incorporating other noncollinear antiferromagnetic
8 materials as the free and fixed layers, and by incorporating alternative insulators such as MgO as
9 the tunnel barrier.

10 We expect that our demonstration of sizeable room-temperature TMR in electrically controlled
11 AATJs on silicon will open new possibilities for a wide range of AFM spintronics experiments.
12 Beyond memory applications, these material structures may also find applications in other devices
13 such as sources and detectors of terahertz radiation^{7, 56-58}, where the output power and detection
14 sensitivity depend on the sensitivity of electrical resistance to changes in the Néel vector.

15 **Acknowledgments:**

16 This work was supported by the National Science Foundation, Division of Electrical,
17 Communications and Cyber Systems (ECCS-2203243, ECCS-1853879, and ECCS-1912694).
18 This work was also supported by the National Science Foundation Materials Research Science and
19 Engineering Center at Northwestern University (NSF DMR-1720319) and made use of its Shared
20 Facilities at the Northwestern University Materials Research Center. This work was also supported
21 by a research contract from Anglo American. One of the magnetic probe stations used in this
22 research was supported by an Office of Naval Research DURIP grant (ONR N00014-19-1-2297).
23 This work utilized the Northwestern University Micro/Nano Fabrication Facility (NUFAB), which
24 is partially supported by the Soft and Hybrid Nanotechnology Experimental (SHyNE) Resource
25 (NSF ECCS-1542205), the Materials Research Science and Engineering Center (NSF DMR-
26 1720139), the State of Illinois, and Northwestern University. This work also made use of the
27 Jerome B. Cohen X-Ray Diffraction Facility supported by the NSF MRSEC program (DMR-
28 1720139) at the Materials Research Center of Northwestern University, and the SHyNE Resource
29 (NSF ECCS-1542205) at Northwestern University. For part of the sample fabrication, use of the
30 Center for Nanoscale Materials, an Office of Science user facility, was supported by the US
31 Department of Energy, Office of Science, Office of Basic Energy Sciences, under contract no. DE-
32 AC02-06CH11357. The work at CSUN was supported by NSF PFI-RP Grant No. 1919109, by
33 NSF ERC-Translational Applications of Nanoscale Multiferroic Systems (TANMS) Grant No.
34 1160504, and by NSF-Partnership in Research and Education in Materials (PREM) Grant No.
35 DMR-1828019. G.F. acknowledges the support from the project “SWAN-on-chip” code
36 101070287, funded by the European Union within the call HORIZON-CL4-2021-DIGITAL-
37 EMERGING-01. The work of G.F. and M.C. has been also supported by the project PRIN
38 2020LWPKH7, funded by MUR (Ministero dell’Università e della Ricerca) within the PRIN 2020
39 call and Petaspin association (www.petaspin.com). V.L.-D. acknowledges the support from the
40 Generalitat Valencia through the CIDEVENT grant CIDEVENT/2022/26.
41

42 **Author contributions:**

1 P.K.A., V. L.-D., J.S., and S.A. designed the devices. J.S., V.L.-D., S.A. and M.H. deposited the
2 material stacks. J.S. and S.A. fabricated the devices. J.S. performed the measurements with support
3 from V.K.S., J.G.A., S.A., M.H., C.A., J.S.J., M.A.G., M.C.H., and H.A.. F.M., J.K. and N.K.
4 performed the *ab initio* calculations. M.C. and G.F. performed the micromagnetic simulations.
5 C.P. performed the HRTEM analysis. J.S., V.L.-D., G.F., F.M., J.K., N.K. and P.K.A. wrote the
6 manuscript with contributions from all the other authors. All authors discussed the results,
7 contributed to the data analysis, and commented on the manuscript. The study was performed
8 under the leadership of P.K.A..

9

10 **Competing interests:**

11 The authors declare no financial or non-financial competing interests.

12

13 **Data and materials availability:**

14 The data that support the findings of this study are available from the corresponding authors upon
15 reasonable request.

16

17 **References**

18 [1] Gomonay, E.; Loktev, V., Spintronics of antiferromagnetic systems. *Low Temperature Physics*
19 **2014**, *40*, 17-35.

20 [2] Olejník, K.; Seifert, T.; Kašpar, Z.; Novák, V.; Wadley, P.; Campion, R. P.; Baumgartner,
21 M.; Gambardella, P.; Němec, P.; Wunderlich, J., Terahertz electrical writing speed in an
22 antiferromagnetic memory. *Science advances* **2018**, *4*, eaar3566.

23 [3] Jungwirth, T.; Marti, X.; Wadley, P.; Wunderlich, J., Antiferromagnetic spintronics. *Nature
24 nanotechnology* **2016**, *11*, 231-241.

25 [4] Jungfleisch, M. B.; Zhang, W.; Hoffmann, A., Perspectives of antiferromagnetic spintronics.
26 *Physics Letters A* **2018**, *382*, 865-871.

27 [5] Wadley, P.; Howells, B.; Železný, J.; Andrews, C.; Hills, V.; Campion, R. P.; Novák, V.;
28 Olejník, K.; Maccherozzi, F.; Dhesi, S., Electrical switching of an antiferromagnet. *Science* **2016**,
29 *351*, 587-590.

30 [6] Puliafito, V.; Khymyn, R.; Carpentieri, M.; Azzerboni, B.; Tiberkevich, V.; Slavin, A.;
31 Finocchio, G., Micromagnetic modeling of terahertz oscillations in an antiferromagnetic material
32 driven by the spin Hall effect. *Physical Review B* **2019**, *99*, 024405.

33 [7] Safin, A.; Puliafito, V.; Carpentieri, M.; Finocchio, G.; Nikitov, S.; Stremoukhov, P.;
34 Kirilyuk, A.; Tyberkevych, V.; Slavin, A., Electrically tunable detector of THz-frequency signals
35 based on an antiferromagnet. *Applied Physics Letters* **2020**, *117*, 222411.

36 [8] Lopez-Dominguez, V.; Almasi, H.; Khalili Amiri, P., Picosecond Electric-Field-Induced
37 Switching of Antiferromagnets. *Physical Review Applied* **2019**, *11*, 024019.

38 [9] Siddiqui, S. A.; Sklenar, J.; Kang, K.; Gilbert, M. J.; Schleife, A.; Mason, N.; Hoffmann,
39 A., Metallic antiferromagnets. *Journal of Applied Physics* **2020**, *128*, 040904.

40 [10] Sengupta, A.; Roy, K., Neuromorphic computing enabled by physics of electron spins:
41 Prospects and perspectives. *Applied Physics Express* **2018**, *11*, 030101.

42 [11] Grzybowski, M.; Wadley, P.; Edmonds, K.; Beardsley, R.; Hills, V.; Campion, R.;
43 Gallagher, B.; Chauhan, J. S.; Novak, V.; Jungwirth, T., Imaging current-induced switching of

1 antiferromagnetic domains in CuMnAs. *Physical review letters* **2017**, *118*, 057701.

2 [12] Godinho, J.; Reichlová, H.; Kriegner, D.; Novák, V.; Olejník, K.; Kašpar, Z.; Šobáň, Z.;
3 Wadley, P.; Campion, R.; Otxoa, R., Electrically induced and detected Néel vector reversal in a
4 collinear antiferromagnet. *Nature communications* **2018**, *9*, 1-8.

5 [13] Bodnar, S. Y.; Šmejkal, L.; Turek, I.; Jungwirth, T.; Gomonay, O.; Sinova, J.; Sapozhnik,
6 A.; Elmers, H.-J.; Kläui, M.; Jourdan, M., Writing and reading antiferromagnetic Mn₂Au by Néel
7 spin-orbit torques and large anisotropic magnetoresistance. *Nature communications* **2018**, *9*, 1-7.

8 [14] Zhou, X.; Chen, X.; Zhang, J.; Li, F.; Shi, G.; Sun, Y.; Saleem, M.; You, Y.; Pan, F.; Song,
9 C., From fieldlike torque to antidamping torque in antiferromagnetic Mn 2 Au. *Physical Review
10 Applied* **2019**, *11*, 054030.

11 [15] Shi, J.; Lopez-Dominguez, V.; Garesci, F.; Wang, C.; Almasi, H.; Grayson, M.; Finocchio,
12 G.; Khalili Amiri, P., Electrical manipulation of the magnetic order in antiferromagnetic PtMn
13 pillars. *Nature Electronics* **2020**, *3*, 92-98.

14 [16] DuttaGupta, S.; Kurenkov, A.; Tretiakov, O. A.; Krishnaswamy, G.; Sala, G.; Krizakova,
15 V.; Maccherozzi, F.; Dhesi, S.; Gambardella, P.; Fukami, S., Spin-orbit torque switching of an
16 antiferromagnetic metallic heterostructure. *Nature communications* **2020**, *11*, 1-8.

17 [17] Arpacı, S.; Lopez-Dominguez, V.; Shi, J.; Sánchez-Tejerina, L.; Garesci, F.; Wang, C.;
18 Yan, X.; Sangwan, V. K.; Grayson, M. A.; Hersam, M. C.; Finocchio, G.; Khalili Amiri, P.,
19 Observation of current-induced switching in non-collinear antiferromagnetic IrMn₃ by differential
20 voltage measurements. *Nature Communications* **2021**, *12*, 3828.

21 [18] Moriyama, T.; Oda, K.; Ohkochi, T.; Kimata, M.; Ono, T., Spin torque control of
22 antiferromagnetic moments in NiO. *Scientific reports* **2018**, *8*, 1-6.

23 [19] Fischer, J.; Gomonay, O.; Schlitz, R.; Ganzhorn, K.; Vlietstra, N.; Althammer, M.; Huebl,
24 H.; Opel, M.; Gross, R.; Goennenwein, S. T., Spin Hall magnetoresistance in
25 antiferromagnet/heavy-metal heterostructures. *Physical Review B* **2018**, *97*, 014417.

26 [20] Meer, H.; Schreiber, F.; Schmitt, C.; Ramos, R.; Saitoh, E.; Gomonay, O.; Sinova, J.;
27 Baldrati, L.; Kläui, M., Direct imaging of current-induced antiferromagnetic switching revealing
28 a pure thermomagnetoelastic switching mechanism in NiO. *Nano Letters* **2020**, *21*, 114-119.

29 [21] Cheng, Y.; Yu, S.; Zhu, M.; Hwang, J.; Yang, F., Electrical Switching of Tristate
30 Antiferromagnetic Néel Order in α - Fe 2 O 3 Epitaxial Films. *Physical Review Letters* **2020**, *124*,
31 027202.

32 [22] Tsai, H.; Higo, T.; Kondou, K.; Nomoto, T.; Sakai, A.; Kobayashi, A.; Nakano, T.;
33 Yakushiji, K.; Arita, R.; Miwa, S.; Otani, Y.; Nakatsuji, S., Electrical manipulation of a
34 topological antiferromagnetic state. *Nature* **2020**, *580*, 608-613.

35 [23] Du, A.; Zhu, D.; Cao, K.; Zhang, Z.; Guo, Z.; Shi, K.; Xiong, D.; Xiao, R.; Cai, W.; Yin,
36 J.; Lu, S.; Zhang, C.; Zhang, Y.; Luo, S.; Fert, A.; Zhao, W., Electrical manipulation and
37 detection of antiferromagnetism in magnetic tunnel junctions. *Nature Electronics* **2023**.

38 [24] Chiang, C.; Huang, S.; Qu, D.; Wu, P.; Chien, C., Absence of evidence of electrical switching
39 of the antiferromagnetic Néel vector. *Physical review letters* **2019**, *123*, 227203.

40 [25] Zhang, P.; Finley, J.; Safi, T.; Liu, L., Quantitative study on current-induced effect in an
41 antiferromagnet insulator/Pt bilayer film. *Physical Review Letters* **2019**, *123*, 247206.

42 [26] Parkin, S. S. P.; Kaiser, C.; Panchula, A.; Rice, P. M.; Hughes, B.; Samant, M.; Yang, S.-
43 H., Giant tunnelling magnetoresistance at room temperature with MgO (100) tunnel barriers.
44 *Nature Materials* **2004**, *3*, 862-867.

45 [27] Yuasa, S.; Nagahama, T.; Fukushima, A.; Suzuki, Y.; Ando, K., Giant room-temperature
46 magnetoresistance in single-crystal Fe/MgO/Fe magnetic tunnel junctions. *Nature Materials* **2004**,

1 3, 868-871.

2 [28] Šmejkal, L.; Sinova, J.; Jungwirth, T., Emerging Research Landscape of Altermagnetism.

3 *Physical Review X* **2022**, *12*, 040501.

4 [29] Mazin, I.; The, P. R. X. E., Editorial: Altermagnetism---A New Punch Line of Fundamental

5 Magnetism. *Physical Review X* **2022**, *12*, 040002.

6 [30] Shao, D.-F.; Zhang, S.-H.; Li, M.; Eom, C.-B.; Tsymbal, E. Y., Spin-neutral currents for

7 spintronics. *Nature Communications* **2021**, *12*, 7061.

8 [31] Bose, A.; Schreiber, N. J.; Jain, R.; Shao, D.-F.; Nair, H. P.; Sun, J.; Zhang, X. S.; Muller,

9 D. A.; Tsymbal, E. Y.; Schlom, D. G.; Ralph, D. C., Tilted spin current generated by the collinear

10 antiferromagnet ruthenium dioxide. *Nature Electronics* **2022**, *5*, 267-274.

11 [32] Dong, J.; Li, X.; Gurung, G.; Zhu, M.; Zhang, P.; Zheng, F.; Tsymbal, E. Y.; Zhang, J.,

12 Tunneling Magnetoresistance in Noncollinear Antiferromagnetic Tunnel Junctions. *Physical*

13 *Review Letters* **2022**, *128*, 197201.

14 [33] Qin, P.; Yan, H.; Wang, X.; Chen, H.; Meng, Z.; Dong, J.; Zhu, M.; Cai, J.; Feng, Z.;

15 Zhou, X.; Liu, L.; Zhang, T.; Zeng, Z.; Zhang, J.; Jiang, C.; Liu, Z., Room-temperature

16 magnetoresistance in an all-antiferromagnetic tunnel junction. *Nature* **2023**, *613*, 485-489.

17 [34] Chen, X.; Higo, T.; Tanaka, K.; Nomoto, T.; Tsai, H.; Idzuchi, H.; Shiga, M.; Sakamoto,

18 S.; Ando, R.; Kosaki, H.; Matsuo, T.; Nishio-Hamane, D.; Arita, R.; Miwa, S.; Nakatsuji, S.,

19 Octupole-driven magnetoresistance in an antiferromagnetic tunnel junction. *Nature* **2023**, *613*,

20 490-495.

21 [35] Liu, Z. Q.; Chen, H.; Wang, J. M.; Liu, J. H.; Wang, K.; Feng, Z. X.; Yan, H.; Wang, X.

22 R.; Jiang, C. B.; Coey, J. M. D.; MacDonald, A. H., Electrical switching of the topological

23 anomalous Hall effect in a non-collinear antiferromagnet above room temperature. *Nature*

24 *Electronics* **2018**, *1*, 172-177.

25 [36] Meir, Y.; Wingreen, N. S., Landauer formula for the current through an interacting electron

26 region. *Physical Review Letters* **1992**, *68*, 2512-2515.

27 [37] Simmons, J. G., Generalized Formula for the Electric Tunnel Effect between Similar

28 Electrodes Separated by a Thin Insulating Film. *Journal of Applied Physics* **1963**, *34*, 1793-1803.

29 [38] Goul, R.; Wilt, J.; Acharya, J.; Liu, B.; Ewing, D.; Casper, M.; Stramel, A.; Elliot, A.;

30 Wu, J. Z., Electron tunneling properties of Al₂O₃ tunnel barrier made using atomic layer

31 deposition in multilayer devices. *AIP Advances* **2019**, *9*, 025018.

32 [39] Wilt, J.; Gong, Y.; Gong, M.; Su, F.; Xu, H.; Sakidja, R.; Elliot, A.; Lu, R.; Zhao, S.;

33 Han, S.; Wu, J. Z., Atomically Thin Al₂O₃ Films for Tunnel Junctions. *Physical Review Applied*

34 **2017**, *7*, 064022.

35 [40] Park, B. G.; Wunderlich, J.; Martí, X.; Holý, V.; Kurosaki, Y.; Yamada, M.; Yamamoto,

36 H.; Nishide, A.; Hayakawa, J.; Takahashi, H., A spin-valve-like magnetoresistance of an

37 antiferromagnet-based tunnel junction. *Nature materials* **2011**, *10*, 347-351.

38 [41] Wang, Y.; Song, C.; Cui, B.; Wang, G.; Zeng, F.; Pan, F., Room-temperature perpendicular

39 exchange coupling and tunneling anisotropic magnetoresistance in an antiferromagnet-based

40 tunnel junction. *Physical review letters* **2012**, *109*, 137201.

41 [42] Wang, Y.; Song, C.; Wang, G.; Miao, J.; Zeng, F.; Pan, F., Anti-Ferromagnet Controlled

42 Tunneling Magnetoresistance. *Advanced Functional Materials* **2014**, *24*, 6806-6810.

43 [43] Wang, X.; Chen, H.; Yan, H.; Qin, P.; Zhou, X.; Meng, Z.; Liu, L.; Liu, X.; Wang, H.;

44 Liu, Z., Room-temperature magnetoresistance in a single-layer composite film based on

45 noncollinear antiferromagnetic Mn₃Sn. *Applied Physics Letters* **2023**, *122*, 152403.

46 [44] Ikeda, T.; Tsunoda, Y., Spin Fluctuations in an Octahedral Antiferromagnet Mn₃Pt Alloy.

1 *Journal of the Physical Society of Japan* **2003**, 72, 2614-2621.
2

3 [45] Šmejkal, L.; González-Hernández, R.; Jungwirth, T.; Sinova, J., Crystal time-reversal
4 symmetry breaking and spontaneous Hall effect in collinear antiferromagnets. *Science Advances*
5 **2020**, 6, eaaz8809.

6 [46] Kota, Y.; Tsuchiura, H.; Sakuma, A., Ab-Initio Study on the Magnetic Structures in the
7 Ordered Mn₃Pt Alloy. *IEEE Transactions on Magnetics* **2008**, 44, 3131-3133.

8 [47] Yu, G.; Upadhyaya, P.; Fan, Y.; Alzate, J. G.; Jiang, W.; Wong, K. L.; Takei, S.; Bender,
9 S. A.; Chang, L.-T.; Jiang, Y.; Lang, M.; Tang, J.; Wang, Y.; Tserkovnyak, Y.; Khalili Amiri,
10 P.; Wang, K. L., Switching of perpendicular magnetization by spin-orbit torques in the absence of
11 external magnetic fields. *Nature Nanotechnology* **2014**, 9, 548-554.

12 [48] You, L.; Lee, O.; Bhowmik, D.; Labanowski, D.; Hong, J.; Bokor, J.; Salahuddin, S.,
13 Switching of perpendicularly polarized nanomagnets with spin orbit torque without an external
14 magnetic field by engineering a tilted anisotropy. *Proceedings of the National Academy of Sciences*
15 **2015**, 112, 10310.

16 [49] Fukami, S.; Zhang, C.; DuttaGupta, S.; Kurenkov, A.; Ohno, H., Magnetization switching
17 by spin-orbit torque in an antiferromagnet–ferromagnet bilayer system. *Nature Materials* **2016**,
18 15, 535-541.

19 [50] Lopez-Dominguez, V.; Shao, Y.; Khalili Amiri, P., Perspectives on field-free spin-orbit torque
20 devices for memory and computing applications. *Journal of Applied Physics* **2023**, 133, 040902.

21 [51] Zheng, Z.; Zhang, Y.; Lopez-Dominguez, V.; Sánchez-Tejerina, L.; Shi, J.; Feng, X.; Chen,
22 L.; Wang, Z.; Zhang, Z.; Zhang, K.; Hong, B.; Xu, Y.; Zhang, Y.; Carpentieri, M.; Fert, A.;
23 Finocchio, G.; Zhao, W.; Khalili Amiri, P., Field-free spin-orbit torque-induced switching
24 of perpendicular magnetization in a ferrimagnetic layer with a vertical composition gradient.
25 *Nature Communications* **2021**, 12, 4555.

26 [52] Razavi, A.; Wu, H.; Shao, Q.; Fang, C.; Dai, B.; Wong, K.; Han, X.; Yu, G.; Wang, K. L.,
27 Deterministic Spin–Orbit Torque Switching by a Light-Metal Insertion. *Nano Letters* **2020**, 20,
28 3703-3709.

29 [53] Huang, Y.-H.; Huang, C.-C.; Liao, W.-B.; Chen, T.-Y.; Pai, C.-F., Growth-Dependent
30 Interlayer Chiral Exchange and Field-Free Switching. *Physical Review Applied* **2022**, 18, 034046.

31 [54] He, W.; Wan, C.; Zheng, C.; Wang, Y.; Wang, X.; Ma, T.; Wang, Y.; Guo, C.; Luo, X.;
32 Stebliy, M. E.; Yu, G.; Liu, Y.; Ognev, A. V.; Samardak, A. S.; Han, X., Field-Free Spin–Orbit
33 Torque Switching Enabled by the Interlayer Dzyaloshinskii–Moriya Interaction. *Nano Letters*
34 **2022**, 22, 6857-6865.

35 [55] Kim, H.-J.; Moon, K.-W.; Tran, B. X.; Yoon, S.; Kim, C.; Yang, S.; Ha, J.-H.; An, K.; Ju,
36 T.-S.; Hong, J.-I.; Hwang, C., Field-Free Switching of Magnetization by Tilting the Perpendicular
37 Magnetic Anisotropy of Gd/Co Multilayers. *Advanced Functional Materials* **2022**, 32, 2112561.

38 [56] Tomasello, R.; Verba, R.; Lopez-Dominguez, V.; Garesci, F.; Carpentieri, M.; Di Ventra,
39 M.; Khalili Amiri, P.; Finocchio, G., Antiferromagnetic Parametric Resonance Driven by Voltage-
40 Controlled Magnetic Anisotropy. *Physical Review Applied* **2022**, 17, 034004.

41 [57] Khymyn, R.; Lisenkov, I.; Tiberkevich, V.; Ivanov, B. A.; Slavin, A., Antiferromagnetic
42 THz-frequency Josephson-like Oscillator Driven by Spin Current. *Scientific Reports* **2017**, 7,
43 43705.

44 [58] Gomonay, O.; Jungwirth, T.; Sinova, J., Narrow-band tunable terahertz detector in
45 antiferromagnets via staggered-field and antidamping torques. *Physical Review B* **2018**, 98,
46 104430.